Dynamic Channel Characteristic Analysis and Modeling of Conductive Intracardiac Communication Based on Sinusoidal Response and Impulse Response

Yu Chen , Yong Xu , Ya Zhou , Xuce Fan , Chang Yang , Yunjia Ge , Yong Song *

Posted Date: 10 April 2026

doi: 10.20944/preprints202604.0730.v1

Keywords: conductive intracardiac communication; dynamic channel characteristics; channel parameters; impulse response

 doi:10.20944/preprints202604.0730.v1

Article

Dynamic Channel Characteristic Analysis and Modeling of Conductive Intracardiac Communication Based on Sinusoidal Response and Impulse Response

Yu Chen [1], Yong Xu [2], Ya Zhou [1], Xuce Fan [1], Chang Yang [1], Yunjia Ge [1] and Yong Song [1,*]

[1] School of Optics and Photonics, Beijing Institute of Technology, Beijing 100081, China
[2] Senior Department of Cardiology, the Sixth Medical Center of PLA General Hospital, Beijing 100048, China
* Correspondence: yongsong@bit.edu.cn (Y.S.)

Abstract

Conductive intracardiac communication (CIC) is one of the most innovative and promising communication technologies in multi-point cardiac pacing schemes that utilize the heart as the transmission channel in recent years. Current research predominantly focuses on the static channel characteristics, with only limited investigations into the dynamic responses of amplitude-frequency and amplitude-time behaviors. Designing CIC systems solely on the basis of static properties can result in inaccurate channel estimation, distorted channel state information (CSI), elevated bit error rate (BER), and overall degradation of system communication performance. To solve the problems of dynamic channel measurement and modeling of the heart, this paper for the first time proposes a dynamic channel modeling method for CIC based on sinusoidal response and impulse response. Firstly, we develop a physical simulation and miniaturized measurement setup to measure dynamic cardiac channel, and analyze the amplitude-frequency characteristics and amplitude-time characteristics. The influence of factors such as instrument differences, heart rate, flow rate and comparative experiments of free electrodes and fixed electrodes on the channel characteristics are also discussed. Secondly, we systematically analyze the path loss, shadowing effect, multipath effect and Doppler effect of the CIC channel. Combined with the dynamic channel characteristics and parameters, we propose a composite fading dynamic channel model and analyze the BER performance of baseband signals transmission and On-Off Keying (OOK) modulation systems. We can conclude that (1) The CIC channel exhibits capacitive characteristics. The fluctuation of the channel gain of the free electrode is mainly caused by motion artifacts. The fixed electrode can effectively suppress this interference. (2) The dynamic channel gain of CIC varies periodically with the heartbeat, and the fluctuation range of the signal is less than 1-2 dB. This is due to the length change of the myocardial tissue. (3) The CIC channel still presents extremely weak shadow fading, no significant multipath, and no measurable Doppler characteristics under dynamic conditions, belonging to an extremely slow fading channel. This work provides effective dynamic channel measurements approach and parameter basis for the transceiver design of CIC and a reliable model for the simulation for CIC systems.

Keywords: conductive intracardiac communication; dynamic channel characteristics; channel parameters; impulse response

1. Introduction

The cardiovascular diseases are among the leading causes of morbidity and mortality worldwide, including coronary heart disease, hypertension, etc. Every year, approximately 18 million people die from such diseases, accounting for 32% of the global total. Leadless cardiac pacemakers (LCP) are implantable devices used to treat heart rhythm disorders that cause heart dysfunction. They stimulate the heart muscle to contract through electrical pulses. Unlike traditional single-chamber right ventricular pacing and wired solutions, subcutaneous implantable cardiac pacemakers and

 doi:10.20944/preprints202604.0730.v1

defibrillators have developed rapidly due to reduced trauma. Dual-chamber pacing systems and cardiac resynchronization therapy (CRT) have gradually matured[1]. In dual-chamber pacing systems, two pacemakers are placed in the right atrium and right ventricle respectively, coordinating their contractions and achieving data synchronization through conductive intracardiac communication technology to ensure normal heart pumping function. The dual-chamber leadless pacemaker must rely on reliable communication. However, the heart is a dynamically moving organ, and static channel modeling can lead to errors in the design of the communication system. Currently, there is a lack of a dynamic channel model that can guide the actual system design.

Conductive intracardiac communication, as a short-distance implantable human body communication technology, utilizes the conductive properties of cardiac muscle tissue and blood to apply electrical signals to the pacemaker electrodes. Most of the current returns to the negative electrode at the transmitting end, while a small portion is received by the positive and negative electrodes at the receiving end, as shown in Figure 1. Compared with traditional radio frequency communication, CIC has advantages such as strong data privacy and low power consumption.

Table 1 lists the currently published research on CIC, classified according to the system construction of CIC, including channel modeling and simulation approach, dynamic circuit model, dynamic channel characteristic studies, signal transmission methods applicable to CIC, and modulation technology.

Table 1. SUMMARY OF CURRENT STUDIES ON CIC

Category	Contents	Work
Channel modeling and simulation approach	Finite element cardiac model and simulation	Mirko Maldari[2]
	Finite element method (FEM) model for tissue	Lukas Bereuter[3]
	Finite-element method, frequency-domain, and finite-difference time-domain (FDTD) in CST	Ali Khaleghi[4]
	HUGO model in CST	Reza Noormohammadi[5]
	A variable-volume finite element cardiac model	Yiming Liu[6]
Dynamic circuit model	A time-varying equivalent circuit model	Ziliang Wei[7]
	A dynamic equivalent circuit model	Dongming Li[8]
	An equivalent circuit model simulating cardiac biomechanical impedance	Han Wang[9]
Dynamic channel characteristics	Dynamic response of amplitude-frequency characteristics below 1 MHz	Lukas Bereuter[3]
	Dynamic response of amplitude-frequency characteristics within 1 MHz-15 MHz	Ali Khaleghi[4]
	Channel gain variations during the cardiac cycle within 10 kHz-10 MHz	Liting Chen[10]
	Compensation method for dynamic channel gain	Dongming Li[11]
CIC data transmission method	In-body and off-body channel path-loss models at 2.4 GHz	Pritam Bose[12]
	Backscatter communication based on conductive coupling	Reza Noormohammadi[5]
Modulation technology	Evaluation of different energy-efficient modulation schemes at 433 MHz	Pritam Bose[13]
	Analysis for optimal communication parameters with On-Off-Keying and Manchester-encoded baseband transmission (BB-MAN)	Adrian Ryser[14]
	A synchronization algorithm to reduce the power consumption of wireless cardiac pacemakers	Adrian Ryser[15]
Dynamic channel modeling approach	Amplitude-frequency characteristic within 100 kHz-1 MHz; Amplitude-time characteristic; Influencing factors: instruments difference, heart rate, flow rate and comparative experiments of free electrodes and fixed electrodes; Path loss; Shadowing effect; Multipath effect; Doppler spread; Dynamic channel modeling	This work

 doi:10.20944/preprints202604.0730.v1

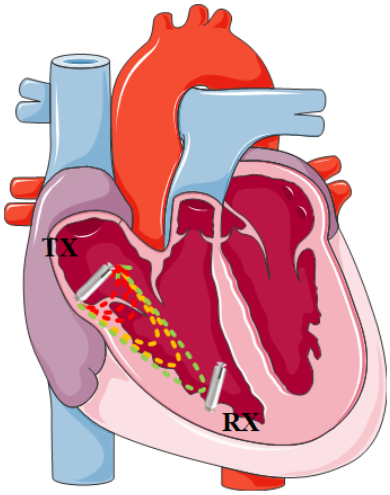

Figure 1. Principle schematic of conductive intracardiac communication. One pacemaker (TX) is placed in the upper or middle part of the right atrium, and the other (RX) is placed at the apex of the right ventricle.

Lukas Bereuter et al. from the University of Bern first proposed the concept of conductive intracardiac communication in 2018. Through finite element simulations and physical experiments, they clarified the characteristics of CIC channels within 1 MHz. Soon they put forward a new concept of leadless cardiac resynchronization therapy and confirmed the feasibility of conductive intracardiac communication[3,16,17].

In the field of channel modeling and simulation approach, Mirko Maldari et al. used a finite element model to clarify the CIC channel attenuation characteristics within the range of 40 kHz to 20 MHz[2]. Ali Khaleghi et al. from Oslo University obtained the CIC channel characteristics in the frequency range of 1 MHz-15 MHz ultilizing Finite-element method (FEM), frequency-domain, and finite-difference time-domain (FDTD), which were verified in a homogeneous phantom and in vivo animal heart experiments[4]. Reza Noormohammadi et al. adopted HUGO model in CST Microwave Studio by including the wideband characteristics of the biological tissues at the frequency range of 300 MHz-500 MHz[5]. Gao Yueming et al. from Fuzhou University established a variable-volume heart model[6].

Although the CIC channel can be simulated using methods such as finite element models, when analyzing the channel gain during heartbeats, the cardiac cycle is divided into individual phases, and the simulated data is obtained in a static state after the cardiac deformation occurs. Additionally, modifying a complex and detailed cardiac electromagnetic model is quite difficult, and the simulation requires extremely high computing power from the computer, with the simulation time being very long.

In the field of circuit modeling, Ziliang Wei et al. establish a time-varying circuit model based on the heart[7], while Dongming Li et al. develop a time-varying circuit model that can be used to simulate both healthy and diseased hearts[8]. Han Wang et al. design a weak-signal measurement circuit with high common mode rejection, and constructed an equivalent circuit model simulating cardiac biomechanical impedance[9].

In the research on dynamic channel characteristics, Lukas Bereuter et al. conducted physical experiments to determine the amplitude-frequency characteristics of CIC within 1 MHz[3]. Ali Khaleghi et al. designed a pulse signal generator and obtained dynamic channel gain at the frequency range of 1 MHz to 15 MHz through in vivo animal heart experiments[4]. Gao Yueming et al. obtained attenuation time curve of a single cardiac cycle at 1 MHz frequency and Channel gain variations during the cardiac cycle within 10 kHz-10 MHz. They provided a set of physical experimental devices for simulating heart beating, by using a peristaltic pump to inject blood into the isolated heart, thereby simulating the blood content and flow rate during heart beating, and further clarifying the influence of factors such as heart volume size, blood content, and flow rate on channel characteristics[10]. Dongming Li et al. propose a dynamic channel gain compensation method[11].

 doi:10.20944/preprints202604.0730.v1

In the field of CIC data transmission methods, Pritam Bose et al. studied the transmission performance in vivo and in vitro at a frequency of 2.4 GHz[12]. Reza Noormohammadi et al. proposed a method of conductive backscatter communication for dual-chamber pacing[5].

Regarding modulation technology aspects, Pritam Bose from University of Oslo and Adrian Ryser from University of Bern evaluated and analyzed different modulation schemes of the CIC system[13,14]. Adrian Ryser et al. propose a synchronization algorithm to reduce the power consumption of wireless cardiac pacemakers[15].

Although these work has made remarkable progress in various research fields, there are still some deficiencies in the research on CIC channels. On the one hand, the static model assumes that the channel remains constant over a period of time, but the real channel is time-varying (such as when the transceivers moves or the environment changes). Relying solely on static characteristics will lead to outdated or distorted channel state information, which cannot reflect the instantaneous channel conditions. Signal processing (such as equalization and demodulation) based on incorrect channel information will significantly increase the bit error rate, reduce throughput and affect communication reliability.

On the other hand, the dynamic characteristics determine the changing pattern of channel quality. Without understanding these changes, key technologies such as adaptive modulation and coding (AMC) and power control will not be able to make timely adjustments, resulting in low spectral efficiency or connection interruptions. The dynamic characteristics also include key parameters such as Doppler frequency shift and time-varying delay spread. Ignoring these factors will prevent the system from coping with frequency-selective fading and time-selective fading, seriously affecting the performance of broadband and high-speed communication systems.

Based on the above analysis, we propose a dynamic channel modeling method for CIC, with the main contributions as follows:

(1) We develop a dynamic channel physical simulation and miniaturized measurement device for CIC for the first time. Motion artifacts and real channel fading are systematically separated in an ex vivo experiments.

(2) The structure of the composite fading model for CIC channels and its key parameters are presented for the first time.

(3) This paper is the first to experimentally confirm that the CIC channel still exhibits extremely weak shadow fading, no significant multipath, and no measurable Doppler shift under dynamic conditions, and is classified as an extremely slow fading channel.

The structure arrangement of the remaining parts of this paper is as follows: The second part describes the measurement methods and principles. The third part analyzes the CIC dynamic channel characteristics and influencing factors. The fourth part analyzes the path loss, shadowing effect, multipath effect and Doppler frequency shift of CIC. The fifth part presents the composite fading dynamic channel model and analyzes its bit error rate and channel capacity. The sixth part analyzes the limitations of the ex vivo experimental device and future work. The seventh part presents the conclusion.

2. Proposed Approaches for Dynamic Channel Measurement

The aim of this paper is not to fully replicate the in vivo physiological environment, but to construct a repeatable and controllable dynamic channel measurement platform for extracting the dynamic characteristics of the CIC channel. Measurements under such well-controlled conditions provide an indispensable foundation for subsequent in vivo research.

The current CIC channel measurement methods mainly rely on vector network analyzers or RF signal sources combined with spectrum analyzers. These instruments are essentially designed for the frequency-domain response of linear time-invariant systems and have three fundamental flaws: (1) The measured dynamic characteristics are composed of data from different phases of the heart. (2) The instrument connected to the circuit board will be grounded to the earth. The battery-powered

 doi:10.20944/preprints202604.0730.v1

transceivers are relatively large in size and will also cause coupling between them, which introduces uncontrollable measurement errors. (3) It cannot be triggered synchronously with the beating heart.

Therefore, the existing studies have actually not obtained the true dynamic channel response, but rather discrete samplings of the static response at different time points. To address this issue, this paper proposes a set of miniaturized, battery-powered, and continuous acquisition physical simulation and measurement devices specifically designed for dynamic channel measurement. For the first time, it has achieved synchronous tracking of amplitude-frequency and amplitude-time characteristics within a complete heart beat.

The principle of dynamic cardiac channel measurement is shown in Figure 2. The dynamic cardiac channel measurement device of CIC consists of two parts: the physical simulation device and the channel measurement device. The physical simulation device mainly includes a temperature-controlled water tank, a pulsating pump and an ex vivo porcine heart.

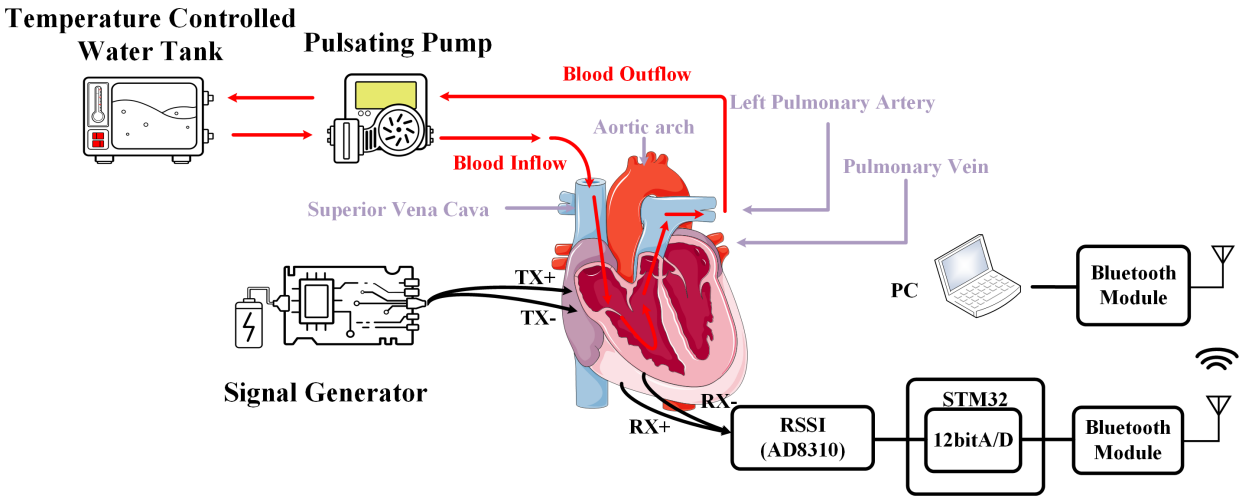

Figure 2. Principle schematic of dynamic channel measurement for CIC.

The temperature-controlled water tank is filled with sterile anticoagulated porcine blood to simulate cardiac blood circulation and the internal environment of the human body.

The pulsation frequency of the pulsating pump is set at 80 beats per minute, the flow rate is 100 mL, and the duty cycle is 50%.

The sterile anticoagulated porcine blood flows out of the temperature-controlled water tank and enters the pulsating pump. From the outlet of the pulsating pump, it enters the superior vena cava through a silicone catheter, then flows from the right atrium to the right ventricle, and flows out from the left pulmonary artery, enters the pulsating pump, and finally flows into the temperature-controlled water tank to achieve the blood circulation and pulse of the heart.

The dynamic channel measurement device includes signal generator, received signal strength indicator (RSSI), STM32, Bluetooth modules and PC.

At the transmitting end, the signal generator can produce sinusoidal signals or pulse signals with adjustable amplitude and frequency. A programmable signal generator based on Direct Digital Synthesis (DDS) technology is constructed around a microcontroller unit (MCU), a DDS chip (AD9850), and associated peripheral circuits, as shown in Figure 3. The system employs a split-rail power supply architecture: an input DC voltage is regulated by two low-dropout linear regulators (LDOs) to generate stable 3.3 V and 5.0 V supplies. Specifically, the AX1117-3.3V LDO powers the STM32F103 microcontroller, while the AX1117-5.0V LDO supplies both the 125 MHz active oscillator and the AD9850 DDS chip.

The 125 MHz active oscillator serves as the reference clock source for the AD9850, connected to its CLK pin, ensuring high frequency resolution in the internal digital waveform generation module. The MCU interfaces with the AD9850 via an 8-bit parallel bus to configure key parameters—including

 doi:10.20944/preprints202604.0730.v1

the frequency tuning word, phase offset, and output amplitude—enabling precise control over the generated signal.

Upon receiving configuration data, the AD9850 synthesizes the corresponding digital waveform. Its integrated DAC simultaneously provides a square wave output and a raw analog output that, after low-pass filtering, yields a sine wave. The square wave is further processed through a duty-cycle adjustment circuit using a resistive voltage divider, enabling variable duty cycle square-wave output. Meanwhile, the sine wave passes through a 75 MHz low-pass filter to suppress harmonic components and is subsequently amplified by an output amplifier to deliver a high-quality analog sine wave signal.

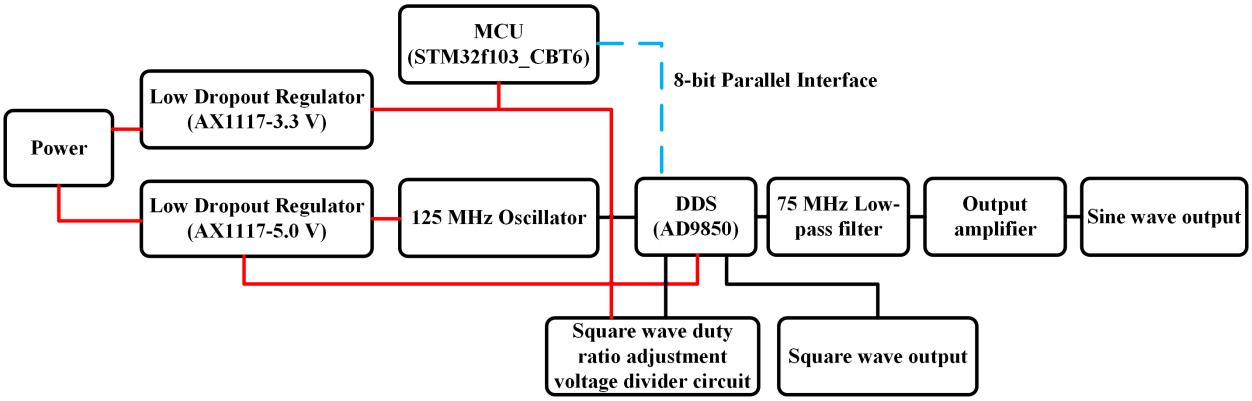

Figure 3. Schematic diagram of the signal generator.

At the receiving end, the power values of the signal is received by the battery-powered RSSI and then transmitted to the PC through the Bluetooth modules which controlled by STM32 for processing of the voltage signal and display.

In this work, the analog voltage output by the RSSI module is converted into digital form by the 10-bit ADC built into the STM32 at a sampling rate of 200 Hz. This sampling rate is 20 times higher than the heart rate and meets the Nyquist sampling requirement, ensuring that the dynamic changes within a heartbeat cycle are not lost. Data acquisition is performed continuously over 120 seconds for each experimental condition. All subsequent channel gain calculations and statistical analyses are based on this continuous dataset. The sampling parameters and post-processing steps are kept consistent across all measurement setups to enable a fair comparison between the proposed DDS-RSSI method and conventional instruments.

The dynamic channel measurement device for ex vivo porcine heart of CIC is shown in Figure 4. To decrease the influence of coupling between the ground of the instrument and the ground electrodes of each device, the signal generator, RSSI and STM32 all adopt battery-powered miniaturized circuit boards.

The positive and negative electrodes at the transmitting end are vertically inserted into the middle of the right atrium, and the positive and negative electrodes at the receiving end are vertically inserted into the middle of the right ventricle.

The needle electrodes are secured to the epicardial surface with an atraumatic 6-0 polypropylene suture tied around the electrode handle. This prevents the needle electrode from loosening or detaching due to cardiac motion, as shown in Figure 5.

The distance between the positive and negative electrodes is 2 cm. The depth of electrode implantation is 8 mm. The transmission distance is 2 cm. All experiments are completed within two hours.

 doi:10.20944/preprints202604.0730.v1

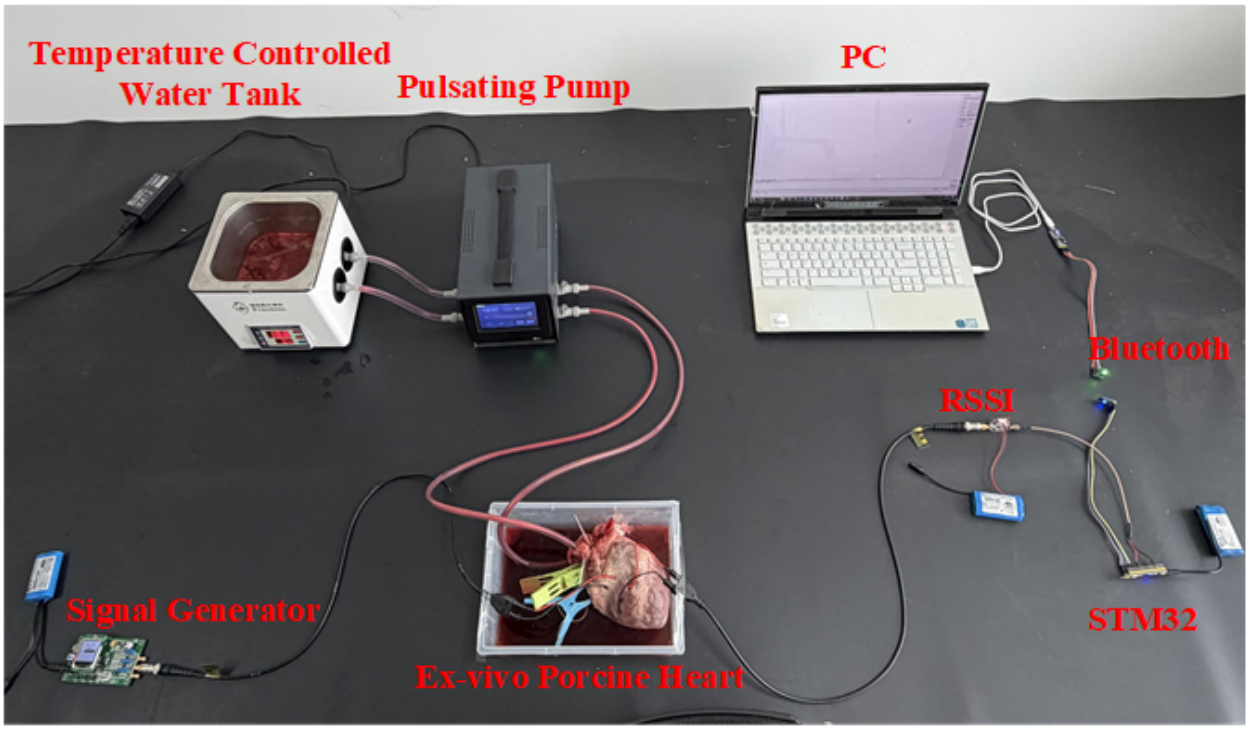

Figure 4. Experimental setup for dynamic channel measurement for CIC. The blue module is a miniaturized lithium battery.

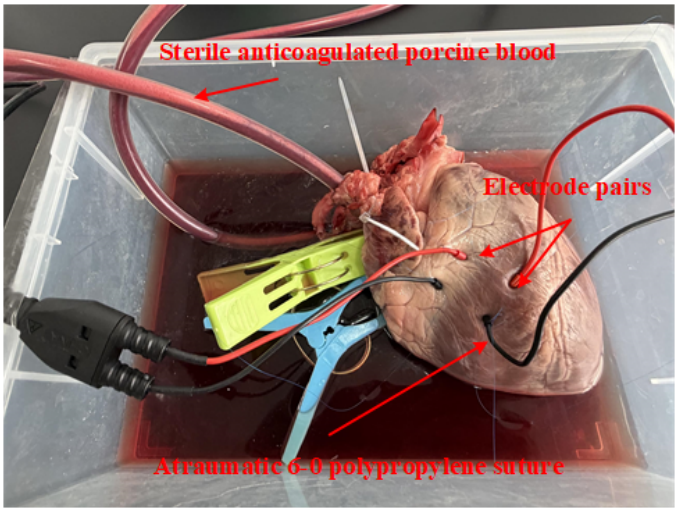

Figure 5. The electrodes are fixed to the surface of the heart through sutures.

3. Dynamic Channel Characteristic Analysis of CIC

3.1. Amplitude-Frequency Characteristic

The relationship between the measured voltage and the received power is shown in Figure 6. It indicates that the voltage does not change with the variation of the carrier frequency, suggesting that the RSSI is stable. The DDS signal generator generates a sinusoidal signal with a peak-to-peak value of 1 V. The frequency is set from 100 kHz to 1 MHz. For amplitude-frequency characteristic measurements, the output frequency of the DDS is increased stepwise. At each frequency point, data are continuously

 doi:10.20944/preprints202604.0730.v1

acquired over no fewer than 10 cardiac cycles, and the average value is then calculated. The received power is calculated using formula (1), and the formula for the channel gain is as formula (2).

$$P_r = 41.4256 \times V_r - 100.5878 \tag{1}$$

$$Gain = P_r - P_0 \tag{2}$$

P_r is the received power, V_r is the received voltage, P_0 is the output power of the signal generator.

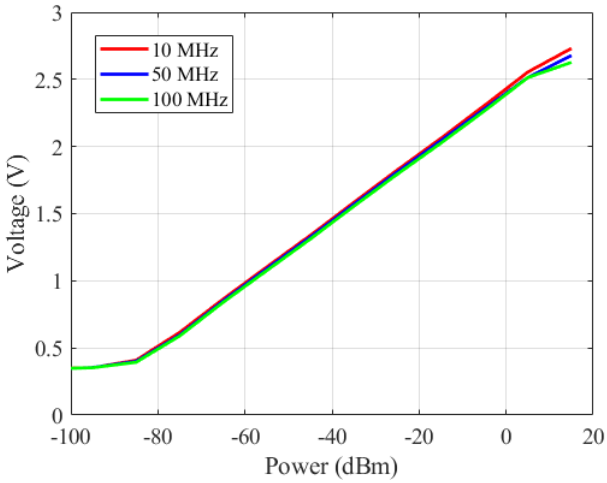

Figure 6. The relationship between received voltage and received power.

The amplitude-frequency characteristics and dynamic response range of CIC are obtained by sinusoidal response. The sinusoidal response results are shown in the Figure 7.

The channel gain of CIC exhibits capacitive coupling characteristics. The average channel gain of CIC increases with the increase of frequency, and the channel gain increases from -54.7 dB to -49.8 dB from 100 kHz to 1MHz.

The vertical intervals at each frequency point represent the fluctuation range of channel gain within one cardiac cycle. Within one heartbeats cycle, the minimum fluctuation of channel gain is 0.7 dB at 700 kHz, and the maximum is 1.62 dB at 200 kHz.

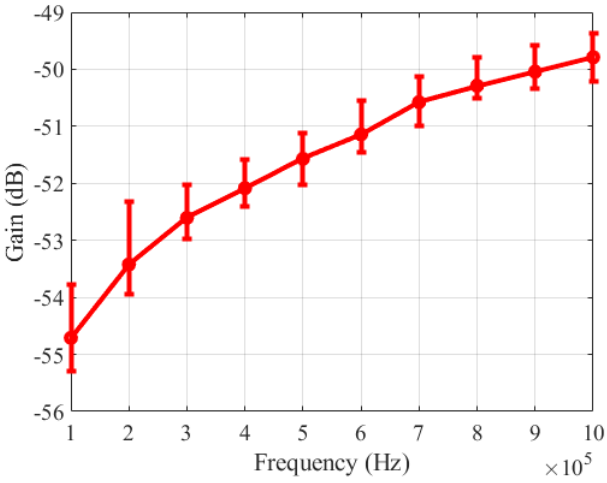

Figure 7. Amplitude-frequency characteristic curve and fluctuation for CIC.

 doi:10.20944/preprints202604.0730.v1

3.2. Amplitude-Time Characteristic

For amplitude-time characteristic measurements, the DDS outputs a fixed frequency, and the system continuously captures data for no less than 120 seconds to extract the dynamic fluctuations within a cardiac cycle.

Figure 8 illustrates the variation in channel gain across the cardiac cycle at different frequencies. It can be clearly observed that the channel gain at low frequencies is less than that at high frequencies. Curves of all frequencies show obvious periodic fluctuations, indicating that the channel gain of CIC varies periodically with the heartbeat movement. The fluctuation is mainly due to periodic length changes in the myocardium induced by the heartbeat.

The fluctuations at low frequencies are larger (1.5 dB at 100 kHz), while they become smaller at higher frequencies (0.8 dB at 1 MHz). This is because the wavelength of low-frequency signals is longer, allowing them to penetrate deeper into the heart. The current covers a larger volume of myocardial tissue, has a longer transmission path, is more affected by overall deformation, and has a high sensitivity to tissue deformation. While high-frequency signals have a shallower penetration depth, they mainly propagate along the surface of the heart, have a shorter path, and are less affected by overall heart deformation.

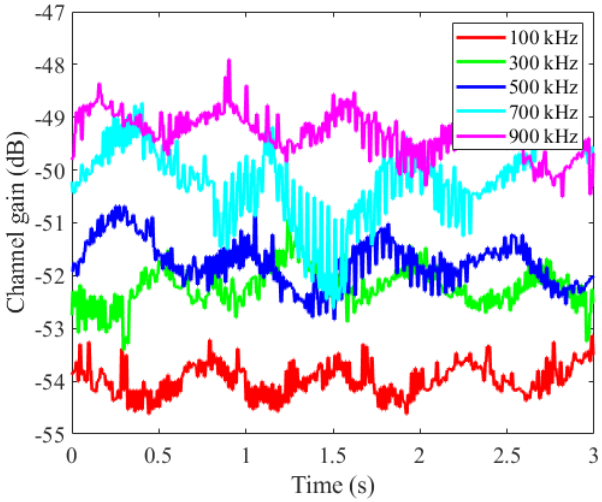

Figure 8. Amplitude-time characteristic curve and fluctuation for CIC.

3.3. Analysis of Influencing Factors on Channel Characteristics

Considering that the experimental results may be affected by various factors, we investigate the influence of different measuring instruments, heart rate and flow rate on the channel characteristics. Additionally, we conduct a control experiment comparing fixed electrodes with free electrodes.

3.3.1. Instruments Difference

To verify the validity and accuracy of the measurement data, we conduct three sets of comparative experiments. Figure 9 presents the channel gains obtained from the three different experimental setups. The red curve represents the results using the DDS signal generator and RSSI method proposed in this paper. The green curve corresponds to measurements taken with RF signal generator and spectrum analyzer. The blue curve shows the data acquired using the vector network analyzer.

 doi:10.20944/preprints202604.0730.v1

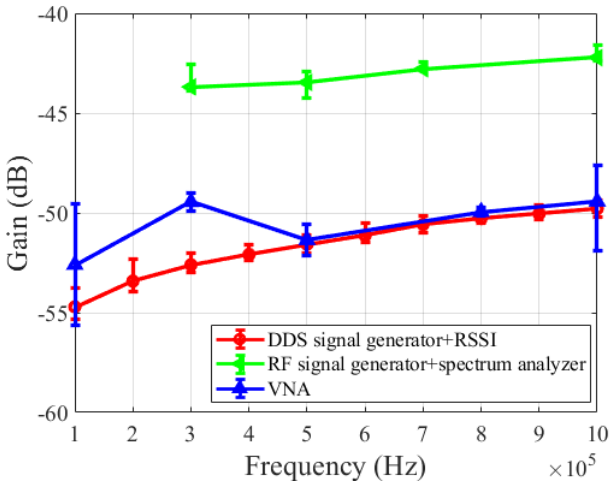

Figure 9. Different experimental instruments for CIC channel measurement. Green curve: The RF signal generator typically limits the minimum output frequency to 250 kHz. Blue curve: The VNA shows significant noise below 1 MHz.

The results show that the channel gain obtained using the DDS signal generator and RSSI ranges from -54.7 dB to -49.8 dB over the frequency range of 100 kHz to 1 MHz.

The channel gain obtained using the RF signal generator and spectrum analyzer ranges from -43.69 dB to -42.22 dB over the frequency range of 300 kHz to 1 MHz, increasing 1.47 dB. The maximum fluctuation amplitude within one cardiac cycle is 1.3 dB, and the minimum fluctuation amplitude is 0.43 dB, with a difference of 0.87 dB.

The channel gain measured using the vector network analyzer range from -52.60 dB to -49.43 dB over the frequency range of 100 kHz to 1 MHz, increasing of 3.17 dB. The maximum fluctuation amplitude within one cardiac cycle is 6.13 dB, and the minimum fluctuation amplitude is 0.4 dB, with a difference of 5.73 dB.

It can be observed that the channel gain trends obtained through these three methods are consistent, and they exhibit capacitive coupling characteristics. The key differences lie in the performance and limitations of each instrument. The experimental configuration using direct digital synthesizer signal generator combined with RSSI module offers high time resolution and stable, continuous data acquisition, making it well-suited for capturing dynamic channel variations within cardiac cycle.

In contrast, measurements using RF signal generator and spectrum analyzer are limited by lower sampling frequency. The RF signal generator (250 kHz-4 GHz) has a minimum output frequency of 250 kHz and cannot produce signals below 250 kHz. Moreover, the RF signal generator and spectrum analyzer are relatively large in size, resulting in stronger coupling to ground and between the instruments themselves, which causes the measured results to be higher than those of the red and blue curves.

The vector network analyzer provides comprehensive frequency-domain data but exhibits higher noise levels at low frequencies. This results in significant data fluctuations and distortion within 100 kHz to 300 kHz, compromising measurement accuracy in the lower band.

The VNA and spectrum analyzer have high noise or a minimum frequency limit in the frequency range below 1 MHz, and their measurement period is much longer than one heart rate cycle. Therefore, the dynamic range is actually the superposition of state differences between different phases, rather than a true dynamic response. The proposed DDS-RSSI system, by cutting off the grounding circuit with battery power supply and using continuous sampling instead of sweep mode, has for the first time achieved point-by-point tracking of channel gain within a continuous heartbeat, eliminating the pseudo-dynamic components introduced by the instrument itself.

 doi:10.20944/preprints202604.0730.v1

3.3.2. Heart Rate

Taking into account that heart rates vary among individuals, we investigate the impact of different heart rates on the channel characteristics. Figure 10 shows the influence of heart rate on channel gain. When the heart rate increases from 40 BPM to 120 BPM, the average channel gain varies within the range of -53.7 dB to -53 dB, with a difference of 0.7 dB.

Within a single cardiac cycle, the maximum fluctuation of channel gain is 1.49 dB at 80 beats/min, and the minimum fluctuation of channel gain is 0.9 dB at 70 beats/min.

These results show that, under normal physiological conditions, the channel remains relatively stable, and the influence of heart rate on channel characteristics is negligible. However, in extreme conditions, channel compensation mechanisms for the CIC system may be necessary.

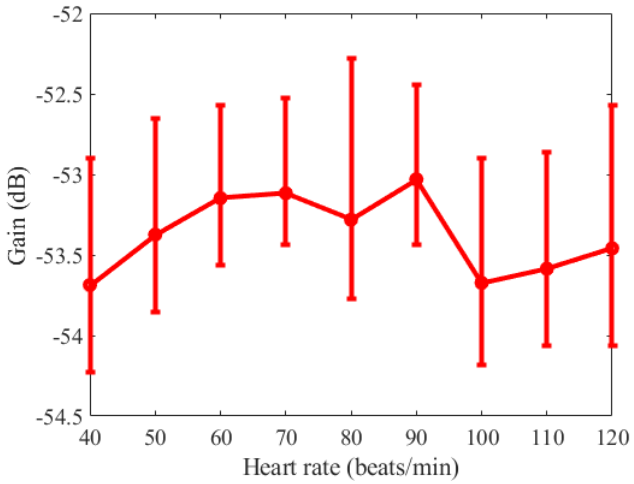

Figure 10. Heart rate on CIC channel characteristics.

3.3.3. Flow Rate

In a resting state, the blood pumping volume of a normal adult's heart is 67-133 ml/s. However, certain cardiovascular diseases such as valve regurgitation, atrial septal defect, and coronary heart disease can cause either excessive or insufficient blood flow in the heart. Therefore, we investigate the impact of heart blood pumping volume on channel characteristics. The formula for calculating the flow rate is as follows.

$$Flow\ Rate = \frac{Stroke\ Volume}{\frac{1}{Heart\ Rate} \times Duty\ Cycle} \tag{3}$$

Figure 11 illustrates the influence of cardiac pumping volume on channel gain. When the blood flow rate changes from 106 ml/s to 266 ml/s, the average channel gain changes from -53.44 dB to -53.88 dB, and the fluctuation range changes from 0.83 dB to 1.53 dB. These experimental results indicate that as blood flow rate increases, the fluctuation range of the channel gain becomes larger, the channel attenuation increases, and the overall channel condition deteriorates.

 doi:10.20944/preprints202604.0730.v1

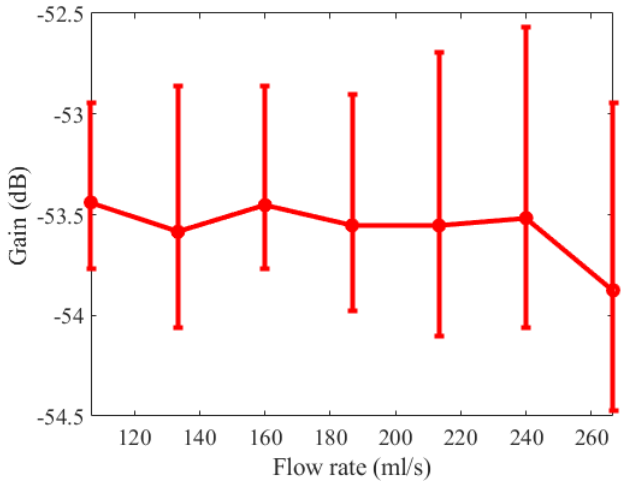

Figure 11. Flow rate on CIC channel characteristics.

3.3.4. Fixed Electrodes vs Free Electrodes

Figure 12 shows the difference in channel gain measured by the free electrodes and the fixed electrodes on the surface of the heart, which is used to analyze the influence of motion artifacts on the signal.

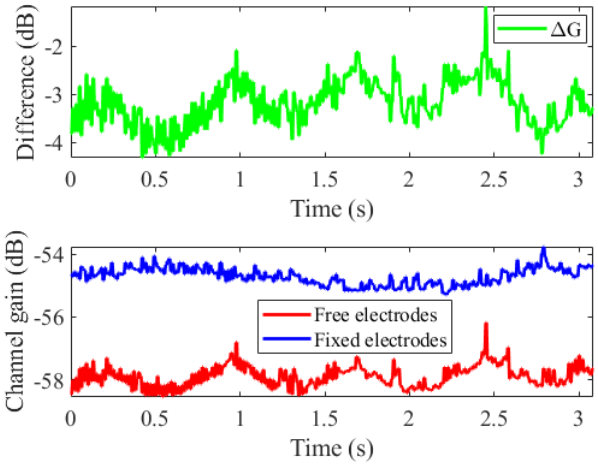

Figure 12. The difference in channel gain measured on the heart surface between the free electrodes and the fixed electrodes.

The red curve represents the channel gain measured by the free electrode, which fluctuates greatly, with an amplitude of 3-4 dB. These fluctuations are synchronized with the heartbeat cycle, indicating that they are motion artifacts caused by the heart beating. The reason is that when the electrode is not fixed, during the contraction of the heart, the electrode is pushed away or the contact area decreases, resulting in an increase in contact impedance and a decrease in channel gain. When the heart is in the relaxation phase, the electrode returns to its original state, and the channel gain recovers.

The blue curve represents the channel gain measured by the fixed electrode, which is relatively stable at <1 dB, indicating that the electrode is firmly fixed and not affected by mechanical movement, and is closer to the true channel response, that is, the true attenuation caused by the real conductivity of the tissue and changes in the geometric path.

The green curve represents the additional gain loss of the free electrode relative to the fixed electrode $\Delta G(t) = G_{\text{free}}(t) - G_{\text{fixed}}(t)$, with a fluctuation amplitude of approximately 2 dB, indicating that motion artifacts cause an additional attenuation of the free electrode signal of about 2-4 dB.

 doi:10.20944/preprints202604.0730.v1

Therefore, we can conclude that the channel gain fluctuations of the free electrode are mainly caused by motion artifacts. The fixed electrode can effectively suppress such interference. $\Delta G(t)$ is a key indicator for evaluating the severity of motion artifacts.

4. Analysis of Channel Fading and Propagation Effects for CIC

4.1. Path Loss

Since the pacemaker is installed at different positions in the heart according to the patient's specific condition, the path loss reduces the average signal energy. We model path loss as a function of distance, with the average path loss following a power-law relationship proportional to the Nth power of distance.

The sinusoidal response experiment is conducted to characterize the variation of path loss with distance. We have established a path loss model based on near-field coupling. Considering the scale of the heart, the transmission distance is varied from 2 cm to 10 cm, and the step is 2 cm with seven measurements recorded at each distance. The fitting curve is derived using the average value at each point to minimize errors arising from measurement variability and experimental fluctuations.

Since the distance between the transmitter and the receiver is very short at the centimeter level, the system is completely within the reactive near-field region. Signals propagate through conductive current and displacement current rather than electromagnetic radiation. The electric field distribution is close to the quasi-static electric field.

From the measurement results in Figure 13, it can be concluded that the voltage attenuation might be slower than $1/d^2$. The increase in path loss gradually slows down as the distance increases. The path loss model uses a logarithmic model:

$$PL_{dB}(d) = PL_0 + \gamma \cdot log_{10}(d/d_0) \tag{4}$$

where $PL_{dB}(d)$ is the path loss in dB, PL_0 is the path loss at d_0, γ is the path loss index.

Figure 13 presents the path loss results and near-field coupling path loss model. As the channel length increases from 2 cm to 10 cm, the path loss increases by 10.96 dB. When γ=15.012, the root mean square error of the model is 0.455. The fitted path loss exponent $n = \gamma/10 \approx 1.5$, indicating that the signal attenuation is weaker than in free space (n=2), and significantly weaker than the theoretical electric dipole field in a conductive medium (n=4). This path loss is consistent with quasi-static field behavior in biological tissues at low frequencies, where current diffusion dominates over radiative effects.

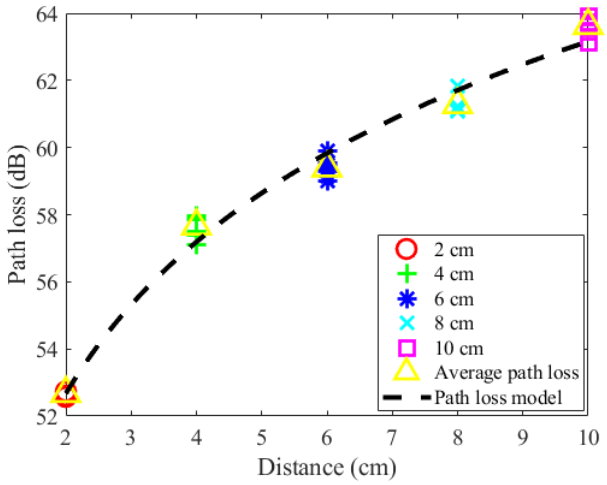

Figure 13. Experimental measurement values, average path loss and path loss model.

 doi:10.20944/preprints202604.0730.v1

4.2. Shadow Fading

In the scenario where both the transmitter and the receiver are located on the beating heart, the shadowing effect is caused by the large-scale signal attenuation resulting from the dynamic occlusion and absorption of the signal due to the deformation of the myocardium, the flow of blood, and the periodic displacement of the surrounding tissues. Therefore, we analyze the dynamic shadowing effect of cardiac physiological modulation.

At the TX side, the signal generator outputs a pulse signal with an amplitude of 5 V, a frequency of 100 kHz, a pulse width of 2 μs, and a duty cycle of 20%. At the RX side, the signal is detected by the RSSI circuit and sampled at 200 Hz by a 10-bit analog-to-digital converter ADC of STM32. The acquired data is sent to the PC through the Bluetooth module of STM32. The heart cycle of the heart is 0.8 s, and a sampling rate of 200 Hz can meet the requirements of channel measurement.

The RSSI collects a total of 138.615 seconds of data. Statistical analysis is conducted on the data within the range of 20 s to 120 s. The snapshots of received power gain ratio is shown in Figure 14. The average received power ratio is -42.4335 dB, and the standard deviation is 0.1842 dB.

In order to analyze the shadowing effect, we conduct statistical analysis of the received power ratio. Firstly, we convert the dB values to the linear domain and fit the received power ratio using eight probability density functions (PDF) such as Normal distribution, Exponential distribution, Weibull distribution, Extreme value distribution, Log-normal distribution, Rayleigh distribution, Nakagami-m distribution, and Rician distribution. The parameters of each distribution are obtained using maximum likelihood estimation, and the Anderson-Darling test is used to determine which distribution best fits the data. The Anderson-Darling statistic is shown in Table 2. According to the results, it is found that the Anderson-Darling statistic of the log-normal distribution is the least, which is most in line with the situation of CIC dynamic channels, and it can be adopted for modeling.

Figure 15 shows the histogram of the power ratio and the probability density function of the log-normal distribution. The channel filter tap h follows the log-normal distribution, which implies that the logarithm of the received power ratio $|h|^2$ follows the normal distribution, $\ln|h|^2 \sim \mathcal{N}(\mu, \sigma^2)$. The probability density function of h can be expressed by the following formula:

$$f(h;\mu,\sigma) = \frac{1}{\sqrt{2\pi}h\sigma} exp[-\frac{(lnh-\mu)^2}{2\sigma^2}] \tag{5}$$

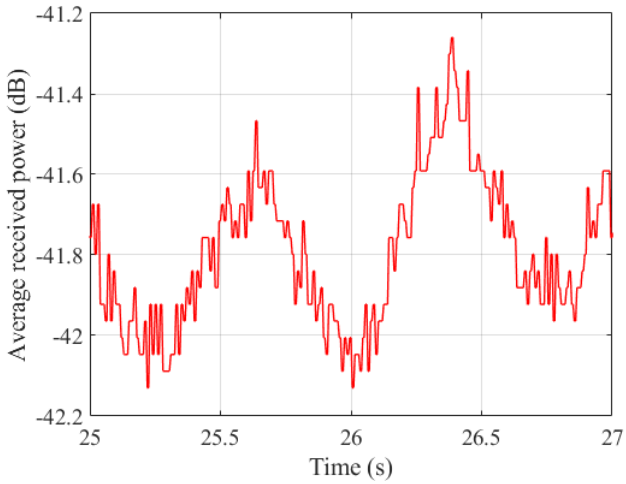

Figure 14. Snapshots of power gain ratio. The RSSI collected a total of 138.615 seconds of data. The data from the 20th second to the 120th second was statistically analyzed. The figure shows the average received power data from the 25th second to the 27th second.

 doi:10.20944/preprints202604.0730.v1

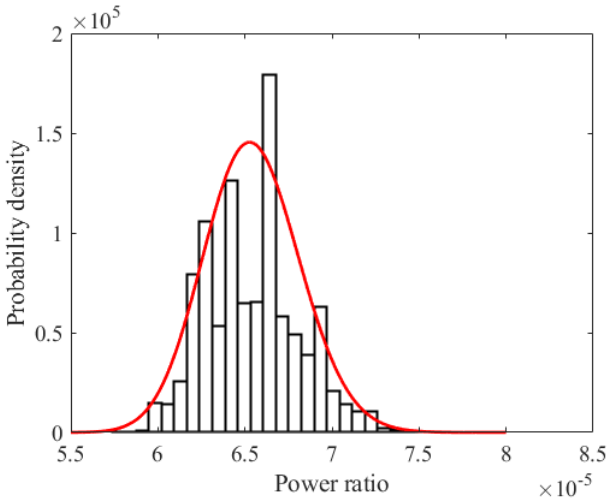

Figure 15. PDF and distribution fits for power ratio. The figure shows a statistical analysis of the average received power from 20 seconds to 120 seconds. Based on the Anderson-Darling test, it is determined that the average received power follows a log-normal distribution.

Table 2. Anderson-darling statistics of various distributions

Distributions	Anderson-Darling statistic
Normal	85.3607
Exponential	3517.8
Weibull	113.3626
Extreme value	117.6824
Log-normal	84.9720
Rayleigh	3369.06
Nakagami-m	549.7009
Rician	28537.8

4.3. Multipath Fading

Multipath fading is caused by the distribution of reflectors and scatterers along the signal transmission path. The multipath effect requires the existence of multiple distinguishable propagation paths. There is a significant time delay difference between each path. The phase of each path signal is random or time-varying, resulting in fluctuations at the receiving end due to coherent superposition of the signals.

According to the fourth-order cole-cole dispersion formula (7)(8)(9)[18], the relative permittivity and conductivity of the heart and blood are shown in the Figures 16 and 17.

$$\hat{\varepsilon}(\omega) = \varepsilon_\infty + \sum_n \frac{\Delta\varepsilon_n}{1 + (j\omega\tau_n)^{(1-\alpha_n)}} + \frac{\sigma_i}{j\omega\varepsilon_0} \tag{6}$$

$$\varepsilon' = \text{real}(\hat{\varepsilon}) \tag{7}$$

$$\sigma = -\,\text{imag}(\hat{\varepsilon}) \cdot \omega \cdot \varepsilon_0 \tag{8}$$

 doi:10.20944/preprints202604.0730.v1

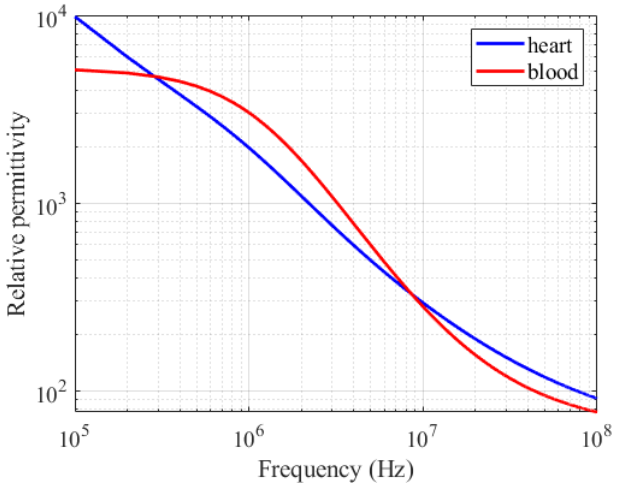

Figure 16. Relative permittivity of blood and the heart from 100 kHz to 100 MHz.

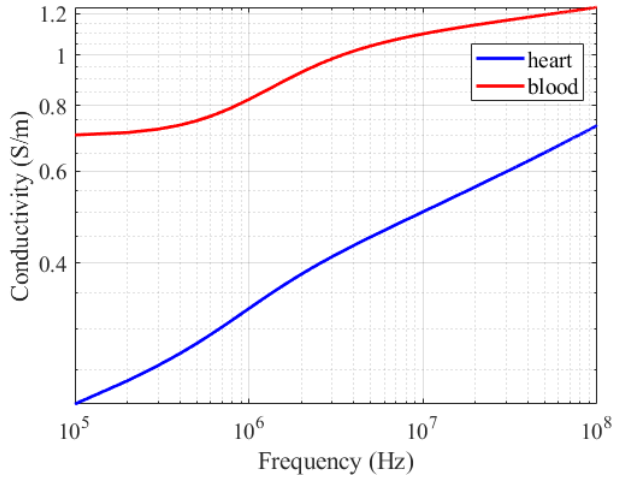

Figure 17. Conductivity of blood and the heart from 100 kHz to 100 MHz.

The high conductivity of the myocardial tissue limits the penetration depth of electromagnetic waves. There are no obvious strong reflection interfaces within the tissue. The dielectric properties of the myocardial tissue gradually change rather than abruptly change, and the reflection coefficient is extremely small. Even if there is a weak reflection, it will be rapidly attenuated by high absorption and cannot form a measurable secondary path.

When the wavelength of the electromagnetic wave is much larger than the size of the heart, the electromagnetic field is in the quasi-static near-field region. Energy is transferred through both conduction current and displacement current. The displacement current originates from the dielectric polarization response of the tissue under the external electric field.

Suppose there are two paths, the length difference ΔL = 0.01 m, The speed of electromagnetic waves in cardiac tissue $v_p \approx c/\sqrt{\varepsilon'}$=3 $\times$ 10^6 m/s, the time delay difference $\Delta\tau = \Delta L/v_p \approx 3.3 \times 10^{-9}$ s $= 3.3$ ns, the corresponding coherent bandwidth $B_c \approx 1/(5\Delta\tau) \approx 60$ MHz, the channel bandwidth is less than 1 MHz. $\Delta\tau \ll 1/B$. All the paths are completely in-phase superimposed at the receiving end, resulting in an enhanced single-path signal with no frequency selectivity and no fading.

4.4. Doppler Fading

Since TX is located in the right atrium and RX in the right ventricle, during the contraction of the heart, the movements of different parts are not synchronized: the atrium contracts first, followed

 doi:10.20944/preprints202604.0730.v1

by the ventricle; the apex of the heart swings with a large amplitude, while the base has a smaller amplitude. The distance between the two points will change periodically.

The physical mechanism of channel fading caused by the relative motion between the transmitter and the receiver due to the beating of the heart is the Doppler effect.

The rate of channel change is represented by the Doppler shift f_d:

$$f_d = \frac{v_{\text{rel}}}{c_{\text{med}}} f_c \tag{9}$$

where f_d is the Doppler shift in Hz, v_{rel} is the relative velocity component (radial velocity) between the transmitters and receivers along the direction of signal propagation, c_{med} is the velocity of wave propagation in the medium, f_c is carrier frequency in Hz.

Suppose the variation range of the transmission and reception distance $\Delta d = 0.01$ m, the heart rate is 1 Hz, approximately representing simple harmonic motion, the maximum velocity $v_{\max} = 2\pi f_{\text{heart}} \cdot \Delta d \approx 0.062\,\text{m/s}$, the maximum Doppler frequency shift $f_d = \frac{v_{\max}}{v_p} f_c \approx 0.002$ Hz. The bandwidth of the CIC signal ranges from several kHz to several MHz. It is simply unable to distinguish such a tiny frequency shift, and the Doppler effect is extremely weak.

Therefore, we conclude that when the heart beats, the contraction and relaxation of the heart cause slight changes in the density and geometry of the local tissues. However, this mainly leads to slow changes in path loss, rather than changes in the multipath structure. Since there are no significant multipath, there will be no fast fading or Doppler spread.

5. Analyze of Composite Fading Dynamic Channel Model for CIC

5.1. Proposed Composite Fading Dynamic Channel Model of CIC

Based on the aforementioned measured data, we a composite fading dynamic channel model of CIC. The parameters of this model are obtained by fitting with the measured data, indicating that it can effectively describe the statistical characteristics of the measured channel. The formula for received power gain is:

$$P_r[m] = \left(10^{-\frac{PL_0+\gamma log_{10}(d/d_0)}{20}} \cdot 10^{\frac{Z(mT_s)}{20}}\right)^2 \cdot P_t + P_n \tag{10}$$

where $P_r[m]$ is the received signal at the m-th sampling moment, T_s is the sampling period, P_t is transmitted power, P_n is noise power.

$$X_{shadow}(mT_s) = 10^{Z(mT_s)/20}, Z(mT_s) \sim N(\mu_{shadow}, \sigma^2_{shadow}) \tag{11}$$

where $X_{shadow}(mT_s)$ is a shadow fading factor in the linear domain, while $Z(mT_s)$ is the shadow fading in dB and follows a normal distribution.

Convert the above formula into dB form:

$$P_r^{(\text{dB})}[m] = P_t^{(\text{dB})} - \left(PL_0 + \gamma \log_{10}\left(\frac{d}{d_0}\right)\right) + Z(mT_s) \tag{12}$$

5.2. BER Analysis for Dynamic Channel Model of CIC

Based on the above results, we further analyze the BER performance of composite fading dynamic channel model of CIC. This simulation is used to demonstrate the trend analysis of system performance under this channel model. The actual BER may vary in specific implementations due to the design of transceivers. According to the 802.15.6 protocol standard [19], we set the transmitted signal as a unipolar baseband pulse signal with an amplitude of 5 V and a pulse width of 2 µs. The cycle is 10 µs and the data rate is 100 kbps. To contrast the performance of communication systems more fairly, we adopt the normalized signal-to-noise (SNR) ratio.

Figure 18 shows the bit error rate performance of single-polarity baseband signals, 100 kHz and 1 MHz carrier frequencies using On-Off Keying modulation. The results indicate that under the

 doi:10.20944/preprints202604.0730.v1

CIC channel conditions, BER of all curves show a general trend of slow decline with the increase of signal-to-noise ratio. Moreover, within the low SNR range, the BER remains at a relatively high level, close to 0.5. Even E_b/E_0=40 dB, the BER is still around 0.14. The above results indicate that the CIC channel has severe fading, mainly due to the combined effect of path loss and shadow fading, which causes significant attenuation of the signal during transmission and relatively strong noise interference, resulting in the difficulty of reducing the BER. When E_b/E_0=40 dB, the BER of OOK modulation with carrier frequencies of 100 kHz and 1 MHz is 0.03 lower than that of the single-polarity baseband signal, while the BER of the 100 kHz and 1MHz carrier frequencies are not significantly different, which indicates that adjusting the carrier frequency has limited effect on improving the BER.

According to E_b/E_0=40 dB and SNR=$10^{SNR_{dB}/10}$, we substitute B=10^6 Hz and SNR=10^4 into C=$Blog_2(1+SNR)$, and C ≈13.29 Mbps, indicating that the maximum rate at which the CIC channel can reliably transmit information is 13.29 Mbps.

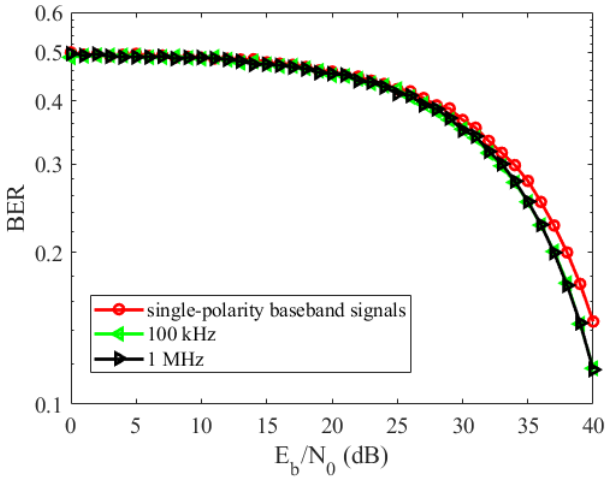

Figure 18. Simulation of BER for baseband signal and OOK modulation with carrier frequencies of 100 kHz and 1 MHz. The simulation is based on the channel parameters measured in this paper.

6. Limitations of Ex Vivo Experiment and Future Work

The experimental data of this paper are obtained through experiments on ex vivo porcine hearts, which can not fully replicate the physiological environment of an in vivo human heart, while offering high experimental repeatability and cost efficiency.

The channel parameters obtained under controlled conditions in this paper provide a baseline model and measurement method basis for the next in-vivo experiments. Subsequently, by simply expanding this platform into a full-heart blood flow model and implanting a micro receiver-transmitter, preclinical validation can be achieved.

Since this paper focuses on the relative fluctuation of channel gain rather than the absolute delay, and the heart beat cycle is approximately 0.8 seconds, which is much longer than the time scale for data acquisition and processing, using the timestamp alignment method can meet the requirements for dynamic characteristic analysis. This measurement system does not achieve hardware synchronization at the receiving and transmitting ends, but since the frequency of channel changes is extremely low, this limitation does not affect the analysis of the channel fluctuation range and statistical characteristics.

In clinical practice, cardiac pacemakers are typically implanted within cardiac chambers; however, in most experimental studies on conductive intracardiac communication, transceivers are placed on the epicardial surface, which remains clinically permissible and widely adopted for feasibility and accessibility.

Future work will focus on implanting miniaturized transceivers into live porcine subjects to conduct in vivo experiments, enabling direct comparison and integrated analysis of data obtained from both in vivo and ex vivo settings. Additionally, we aim to capture the full complex signal, including its

 doi:10.20944/preprints202604.0730.v1

phase information. Leveraging the periodic modulation of channel gain induced by cardiac motion, we will propose a low-duty-cycle coding or modulation scheme tailored to exploit these dynamic characteristics, thereby facilitating energy-efficient, low-power data transmission for implantable cardiac devices.

7. Conclusion

This paper firstly propose a dynamic channel modeling method for CIC based on sinusoidal response and impulse response. We develop a physical simulation and miniaturized measurement setup to measure dynamic cardiac channel for the first time. Motion artifacts and real channel fading are systematically separated in an ex vivo experiments. The structure of the composite fading model for CIC channels and its key parameters are presented for the first time.

Because this device eliminates issues such as grounding coupling, motion artifacts, and mismatch in measurement time scales, it is able to reveal the true characteristics of the CIC channel under dynamic conditions for the first time, including extremely low shadow fading (0.18 dB) and undetectable Doppler. If traditional instruments are used, these characteristics would be masked by instrument noise and grounding interference.

Currently, a few of preliminary conclusions of the CIC channel has been achieved: (1) The CIC channel exhibits capacitive characteristics. The fluctuation of the channel gain of the free electrode is mainly caused by motion artifacts. The fixed electrode can effectively suppress this interference. (2) The dynamic channel gain of CIC varies periodically with the heartbeat, and the fluctuation range of the signal is less than 1-2 dB. This is due to the length change of the myocardial tissue. (3) The CIC channel presents extremely weak shadow fading, no significant multipath, and no measurable Doppler characteristics under dynamic conditions, belonging to an extremely slow fading channel.

Author Contributions: Conceptualization, methodology, validation, data curation, writing-original draft preparation, Y.C.; formal analysis, Y.X. and Y.Z.; software programming, X.F., C.Y. and Y.G.; supervision, methodology, experimental validation, funding acquisition and writing, review and editing, Y.S..

Funding: This work is the results of the research project funded by the National Natural Science Foundation of China General Program (under Grant 82272130), in part by the National Natural Science Foundation of China Key Program (under Grant U22A20103).

Data Availability Statement: The data presented in this study are available on request from the corresponding author. The data are not publicly available due to privacy.

Acknowledgments: Special thanks to Dr. Xu Zhang for his support during the writing of this paper.

Conflicts of Interest: The authors declare that they have no known competing financial interests or personal relationships that could have appeared to influence the work reported in this paper.

References

1. Saleem-Talib, S.; Hoevenaars, C.P.; Molitor, N.; van Driel, V.J.; van der Heijden, J.; Breitenstein, A.; van Wessel, H.; van Schie, M.S.; de Groot, N.M.; Ramanna, H. Leadless pacing: a comprehensive review. *European Heart Journal* **2025**, *46*, 1979–1990.
2. Maldari, M.; Albatat, M.; Bergsland, J.; Haddab, Y.; Jabbour, C.; Desgreys, P. Wide frequency characterization of intra-body communication for leadless pacemakers. *IEEE Transactions on Biomedical Engineering* **2020**, *67*, 3223–3233.
3. Bereuter, L.; Kuenzle, T.; Niederhauser, T.; Kucera, M.; Obrist, D.; Reichlin, T.; Tanner, H.; Haeberlin, A. Fundamental characterization of conductive intracardiac communication for leadless multisite pacemaker systems. *IEEE transactions on biomedical circuits and systems* **2018**, *13*, 237–247.
4. Khaleghi, A.; Noormohammadi, R.; Balasingham, I. Conductive impulse for wireless communication in dual-chamber leadless pacemakers. *IEEE Transactions on Microwave Theory and Techniques* **2020**, *69*, 443–451.
5. Noormohammadi, R.; Khaleghi, A.; Bergsland, J.; Balasingham, I. Conductive backscatter communication for dual-chamber leadless pacemakers. *IEEE Transactions on Microwave Theory and Techniques* **2022**, *70*, 2442–2450.

 doi:10.20944/preprints202604.0730.v1

6. Liu, Y.; Gao, Y.; Chen, L.; Liu, T.; Yang, J.; Pun, S.; Vai, M.; Du, M. A variable-volume heart model for galvanic coupling-based conductive intracardiac communication. *Sensors* **2022**, *22*, 4455.
7. Wei, Z.; Wang, H.; Li, D.; Vai, M.I.; Pun, S.H.; Yang, J.; Du, M.; Gao, Y. A Time-Varying Equivalent Circuit Modeling and Measuring Approach for Intracardiac Communication in Leadless Pacemakers. *IEEE Transactions on Biomedical Circuits and Systems* **2024**, *18*, 872–884. https://doi.org/10.1109/TBCAS.2024.3360997.
8. Li, D.; Wang, J.; Wang, H.; Huang, X.; Yang, J.; Gao, Y.; Li, H.C.; Vai, M.I.; Pun, S.H. A Dynamic High-Fidelity Equivalent Circuit Phantom for Intracardiac Communication in Pacemaker Indications. *IEEE Transactions on Instrumentation and Measurement* **2025**, *74*, 1–12. https://doi.org/10.1109/TIM.2025.3555701.
9. Wang, H.; Li, D.; Vai, M.I.; Pun, S.H.; Yang, J.; Li, H.C.; Gao, Y. Analysis and Circuit Design of Imbalanced Impedance Channels for Conductive Intracardiac Communication. *IEEE Transactions on Biomedical Circuits and Systems* **2025**, *19*, 815–826. https://doi.org/10.1109/TBCAS.2024.3504832.
10. Chen, L.; Liu, Y.; Chen, Z.; Pun, S.H.; Vai, M.I.; Gao, Y. An investigation on conductive intracardiac communication dynamic channel gain during the cardiac cycle for leadless pacemakers. *IEEE Journal of Electromagnetics, RF and Microwaves in Medicine and Biology* **2022**, *7*, 82–89.
11. Li, D.; Wang, Z.; Wang, H.; Hang Pun, S.; Un Mak, P.; Zhang, A.; Liu, Y.; Li, H.C.; Gao, Y.; Du, M.; et al. Dynamic Path Gain Compensation for Enhancing Intracardiac Communication in Leadless Pacemakers. *IEEE Transactions on Instrumentation and Measurement* **2025**, *74*, 1–11. https://doi.org/10.1109/TIM.2025.3551478.
12. Bose, P.; Khaleghi, A.; Balasingham, I. In-body and off-body channel modeling for future leadless cardiac pacemakers based on phantom and animal experiments. *IEEE Antennas and Wireless Propagation Letters* **2018**, *17*, 2484–2488.
13. Bose, P.; Khaleghi, A.; Mahmood, S.; Albatat, M.; Bergsland, J.; Balasingham, I. Evaluation of data telemetry for future leadless cardiac pacemaker. *IEEE Access* **2019**, *7*, 157933–157945.
14. Ryser, A.; Schmid, T.; Bereuter, L.; Burger, J.; Reichlin, T.; Niederhauser, T.; Haeberlin, A. Modulation scheme analysis for low-power leadless pacemaker synchronization based on conductive intracardiac communication. *IEEE transactions on biomedical circuits and systems* **2022**, *16*, 419–429.
15. Ryser, A.; Baeriswyl, C.; Moser, M.; Burger, J.; Reichlin, T.; Niederhauser, T.; Haeberlin, A. A Direct-Digital 40 μA 100 kb/s Intracardiac Communication Receiver With 250 μs Startup Time for Low Duty-Cycle Leadless Pacemaker Synchronization. *IEEE Transactions on Biomedical Circuits and Systems* **2024**, *18*, 1338–1353. https://doi.org/10.1109/TBCAS.2024.3390620.
16. Bereuter, L.; Niederhauser, T.; Kucera, M.; Loosli, D.; Steib, I.; Schildknecht, M.; Zurbuchen, A.; Noti, F.; Tanner, H.; Reichlin, T.; et al. Leadless cardiac resynchronization therapy: An in vivo proof-of-concept study of wireless pacemaker synchronization. *Heart rhythm* **2019**, *16*, 936–942.
17. Bereuter, L.; Gysin, M.; Kueffer, T.; Kucera, M.; Niederhauser, T.; Fuhrer, J.; Heinisch, P.; Zurbuchen, A.; Obrist, D.; Tanner, H.; et al. Leadless dual-chamber pacing: a novel communication method for wireless pacemaker synchronization. *JACC: Basic to Translational Science* **2018**, *3*, 813–823.
18. Gabriel, S.M.; Lau, R.W.; Gabriel, C. The dielectric properties of biological tissues: III. Parametric models for the dielectric spectrum of tissues. *Physics in medicine and biology* **1996**, *41 11*, 2271–93.
19. Ieee, B.E. IEEE Standard for Local and metropolitan area networksPart 15.6: Wireless Body Area Networks. *IEEE* **2012**.